

Scaling turbulent dissipation in an Arctic fjord

Ilker Fer*

Bjerknes Centre for Climate Research & Geophysical Institute, University of Bergen, Allegaten 70, N-5007, Bergen, Norway

Accepted 6 December 2005

Abstract

In September 2003, microstructure and fine-scale shear (vertical derivative of horizontal current) and strain (vertical derivative of isopycnal displacements) profiles were collected in Storfjorden, Svalbard Archipelago. Storfjorden is a sill-fjord of significant dense water production and the period of observations corresponds to weak overflow conditions of the dense water. The data set comprises fine-scale measurements combined with simultaneous dissipation and buoyancy frequency profiles and allows for evaluation of various turbulence scalings and internal wave–wave interaction models. Microstructure profiles identified high levels of background vertical diffusivity, K_ρ , $O(10^{-4})\text{m}^2\text{s}^{-1}$, which increased by one order within the overflow. Fine-scale shear and strain spectral levels were found to be elevated above those of Garrett–Munk, consistent with the observed enhanced mixing, whereas their average ratio was comparable to that of Garrett–Munk. Among the internal wave–wave interaction models, a shear–strain model agreed with the observations (between the surface and bottom mixed layers) within a factor of 2, on the average. A scaling of the dissipation, ε , in the form of total-energy $\times N$ suggests that approximately 0.5% of the energy is dissipated per buoyancy period, $2\pi/N$. The best-fit power-law scaling between diffusivity and N is $K_\rho \propto N^{-1.4 (\pm 0.2)}$. For this environment, a parameterization of the form of Pacanowski–Philander is suggested with background levels of eddy viscosity and diffusivity elevated by an order of magnitude.

© 2006 Elsevier Ltd. All rights reserved.

Keywords: Turbulence; Mixing; Dissipation; Internal waves; Storfjorden

1. Introduction

With an aim to better quantify the marine climate processes in the polar marginal seas, a multi-investigator project “Polar Ocean Climate Processes” (ProClim) was initiated with geographical emphasis on the western Barents Sea, Svalbard region, and Greenland Sea. In one of the four work packages, microstructure measurements in

Storfjorden in Svalbard Archipelago (Fig. 1) were foreseen in order to evaluate and attempt to parameterize the background mixing rate and that associated with the dense overflow plume dynamics.

Storfjorden is a sill-fjord¹ of significant dense water production in winter. The dense water is of

¹Two narrow and shallow (<50 m deep) straits in the North connect the basin with the northwestern Barents Sea. The basin is therefore not strictly a fjord by definition; however, the straits are not significant for the dynamics of the basin, especially when they are ice covered in winter.

*Tel.: +47 55 58 25 80; fax: +47 55 58 98 83.

E-mail address: ilker.fer@gfi.uib.no.

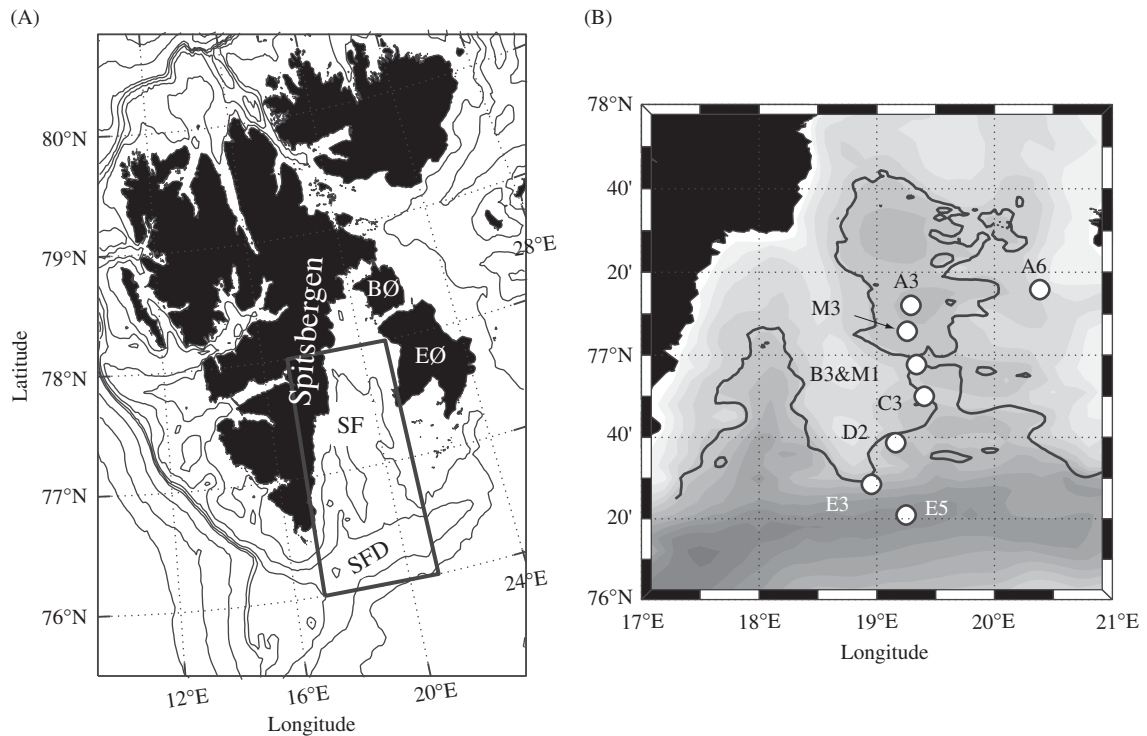


Fig. 1. Location map showing Storfjorden (SF), and the surrounding islands Spitsbergen, Edgeøya (EØ), and Barentsøya (BØ). SFD indicates Storfjordrenna. The rectangle in (A) is enlarged in (B). Isobaths (ETOPO2) and are drawn at 100-m intervals to 500 m and at 500-m intervals to 3000 m in (A) and at 25-m intervals in (B). The additional 125-m isobath (black) in (B), derived from the 500×500 m resolution bathymetry presented in Skogseth et al. (2005b), is included to identify the sill. The microstructure stations (circles) occupied by R.V. *G. O. Sars* during September 2003 are shown with names indicated. Stations B3 and M1 are at the 115-m deep sill, which extends eastwards along 77°N .

brine origin and is formed in a recurring latent-heat polynya² of considerable ice production. The site is considered as a “climate laboratory” in which many of the climate-related oceanic processes (e.g., air–ice–ocean interaction, shelf convection, and overflow dynamics) can be studied in the field and contrasted with regional model results. Because the overflow of the dense water originating in Storfjorden is occasionally traced in the deep Fram Strait (Quadfasel et al., 1988), it is considered to contribute to the ventilation of the deep Arctic Ocean. The ultimate depth that the plume will detach from the bottom will be controlled by the mixing, hence the entrainment, it encounters. It is therefore important to understand and attempt to parameterize the mixing in this laboratory.

²A polynya is an opening (ice-free, very little or only thin ice) enclosed in sea ice. Latent heat polynya is formed and maintained open by advection of ice by tidal currents or offshore winds. A recurring polynya forms at the same location every year.

Away from the boundaries, in the stratified ocean interior, the internal wave continuum (frequencies between the local inertial frequency, f , and the local buoyancy frequency, N) is reasonably well represented by the empirical wavenumber–frequency model of Garrett–Munk (Garrett and Munk, 1972, GM in the following). This simple representation allowed relating mixing rates to larger-scale observable parameters, e.g., shear (vertical derivative of horizontal velocity) and strain (vertical derivative of isopycnal displacement) through models employing nonlinear wave–wave interactions (Section 2.2). Away from boundaries, successful parameterizations capture the observed levels of dissipation within a factor of two for both GM (Gregg, 1989) and (with appropriate corrections) non-GM conditions of the ocean (Polzin et al., 1995). Enhanced mixing rates over the rough topography of the Southern Ocean is recently predicted by inferring mixing rates from fine-scale shear and strain (Naveira Garabato et al., 2004b). Similar techniques were used to map the turbulent diapycnal mixing in the Nordic Seas

(Naveira Garabato et al., 2004a). On the continental slope and shelf and in the marginal seas the applicability of the GM model is uncertain (Levine, 2002); however, it is useful to compare the shelf internal wave field to that of the deep ocean and test the applicability of the associated turbulence scalings.

In this paper, we present dissipation measurements in Storfjorden and Storfjordrenna (Fig. 1) and compare our observations to the values inferred from fine-scale shear and strain field. The data set is minute for parameterization purposes; nevertheless it comprises the first direct turbulence measurements in the vicinity. Our primary goal is to validate and provide applicable parameterizations of sub-grid scale mixing for regional modeling envisaged for the site. We seek answers to the questions: What are the typical background shear and strain levels and how do they compare to the GM field? What is the turbulent dissipation and vertical diffusivity associated with the dense overflow plume and the ambient waters? How well do the existing internal wave–wave interaction parameterizations represent the observed levels of background mixing? What is the typical shear-to-strain ratio in this basin–sill–ocean system at this high latitude where the semi-diurnal internal waves may not propagate freely?

2. Background

2.1. The Garrett and Munk spectrum

The GM spectrum (Garrett and Munk, 1972, 1975) is an empirical wavenumber–frequency model spectrum of the internal wave field, derived from observations. It is used as a representative statistical description of the internal wave field in studies of mixing parameterizations (Henyey et al., 1986; Gregg, 1989; Polzin et al., 1995). We therefore give a brief summary for completeness.

Away from the proximity to boundaries, the internal wave spectrum appears to have a universal shape and energy level, thought to be maintained by rapid and significant nonlinear internal wave interactions. Such interactions efficiently redistribute energy and momentum, thereby relaxing any distortion of the spectral shape rapidly towards this universal shape. The GM spectrum is isotropic in the horizontal (i.e. no dependence on the direction) and is formulated as separable functions of frequency, ω , and mode number, j (or vertical wavenumber) for an exponentially stratified ocean, $N(z) = N_0 e^{z/b}$. The

canonical values are $N_0 = 5.24 \times 10^{-3} \text{ s}^{-1}$ ($\equiv 3$ cycles per hour, cph) and $b = 1300 \text{ m}$, e-folding scale of $N(z)$ (i.e. wave guide thickness).

In the following we will employ GM76 (Garrett and Munk, 1975; as modified by Cairns and Williams, 1976) without adjusting the canonical parameters for the site and observations (see Section 5.1 for discussion). This is further revised by Munk (1981) resulting in variances of shear and strain $2/\pi$ times smaller than those from GM76 (for discussion see Appendix in Gregg and Kunze, 1991). In GM76 as presented by Gregg and Kunze (1991), the vertical wavenumber spectra of vertical isopycnal displacement, ζ , and of horizontal velocity, $V(u, v)$ with u, v components of the horizontal velocity, are³

$$\Phi_{\zeta}(\beta) = \frac{E_{\text{GM}} b^3}{2\pi j_*} \left(\frac{N_0}{N}\right)^2 \frac{1}{(1 + \beta/\beta_*)^2} \left[\frac{\text{m}^2}{\text{rad m}^{-1}} \right], \quad (1)$$

$$\Phi_V(\beta) = \frac{3E_{\text{GM}} b^3}{2\pi j_*} N_0^2 \frac{1}{(1 + \beta/\beta_*)^2} \left[\frac{\text{m}^2 \text{s}^{-2}}{\text{rad m}^{-1}} \right]. \quad (2)$$

Here $E_{\text{GM}} = 6.3 \times 10^{-5}$ and j_* (typically taken as 3) are the dimensionless spectral level and the reference mode number for GM, respectively. The reference wavenumber is $\beta_* = (\pi j_*/b)(N/N_0) \text{ rad m}^{-1}$. For wavenumbers greater than a cut-off wavenumber, β_c (typically $\beta_c = 0.6 \text{ rad m}^{-1}$ or $k_c = 0.1$ cycles per meter, cpm), $\Phi_{\zeta}(\beta) = \Phi_{\zeta}(\beta)(\beta_c/\beta)$ and $\Phi_V(\beta) = \Phi_V(\beta)(\beta_c/\beta)$ to account for the roll-off observed for the temperature (Gregg, 1977) and shear spectra (Garrett et al., 1981). The spectra of vertical strain, $\zeta_z = \partial\zeta/\partial z$, and shear, $V_z (\partial u/\partial z, \partial v/\partial z)$ can be derived by multiplying the displacement and total horizontal velocity spectra, respectively, by wavenumber squared. The GM76 variances for strain and shear integrated to an upper cutoff wavenumber $\beta_c = 0.6 \text{ rad m}^{-1}$ (10 m vertical scale) are 0.23, and $0.69N^2$, respectively (accurate to within 10% for $\beta_c > 10\beta_*$). The shear spectra are often normalized by the mean buoyancy frequency, referred to as Froude spectra, in order to account for varied stratifications. The shear-to-strain ratio (incorporating N -normalized shear) is

$$R_{\omega} = \frac{V_z^2}{N^2 \zeta_z^2}, \quad (3)$$

³Following Gregg and Kunze (1991), the analytic forms are given in radian wavenumber, β and are converted to cyclic units by $k = \beta/2\pi$ and by multiplying the spectra by 2π in order to preserve the spectral variances.

where R_ω is commonly interpreted as the ratio of horizontal kinetic to available potential energy and $R_\omega = 3$ for the GM prescription. Averaged over a single wave's phase with frequency ω , $R_\omega \equiv [(N^2 - \omega^2)(\omega^2 + f^2)]/[N^2(\omega^2 - f^2)]$, where f is the inertial frequency. At 77°N , lunar semidiurnal frequency, M_2 , internal waves cannot propagate freely ($\omega_{M_2} > f$), but, e.g., R_ω is about 44 and 1.7 for the solar semidiurnal tide, S_2 , and M_4 ($\equiv 2M_2$), respectively.

2.2. Dissipation parameterizations inferred from internal wave–wave interactions

Theoretical nonlinear internal wave–wave interaction models (McComas and Müller, 1981; Henyey et al., 1986) are often used to estimate dissipation rates assuming a net energy flux into the higher vertical wavenumbers of a statistically stationary model spectrum (typically GM). Different models imply that turbulent dissipation, ε , associated with GM levels is $O(10^{-9}) \text{ W kg}^{-1}$ and using Osborn's model (Osborn, 1980), $K_\rho = \Gamma\varepsilon/N^2 = 5 - 10 \times 10^{-6} \text{ m}^2\text{s}^{-1}$, (employing N_0 and a typical value of $\Gamma = 0.2$). Levels of shear and strain above the GM model will yield enhanced mixing rates.

In his pioneering work, Gregg (1989, referred to as G89) proposed an estimate of ε as a simple function of buoyancy frequency and 10-m finite-differenced shear observations:

$$\varepsilon_{\text{G89}} = 7 \times 10^{-10} \frac{\langle N^2 \rangle}{N_0^2} \frac{\langle V_z^4 \rangle_{10}}{\langle V_z^4 \rangle_{\text{GM}}} \quad [\text{W kg}^{-1}]. \quad (4)$$

Here and in the following brackets indicate an appropriate averaging procedure (spatial or ensemble average). Gregg compared his inferences to two different approaches based on wave-triad (McComas and Müller, 1981, referred to as MM) and ray-tracing (Henyey et al., 1986, referred to as HWF) internal wave–wave interaction theory. The MM model is based on resonant interaction theory in which energy and momentum can be transferred between internal wave triads with two mechanisms⁴ each diffusing wave action in wavenumber space. In steady state, the total flux through the internal wave spectrum equals the turbulent energy dissipation.

⁴Parametric sub-harmonic instability (decay of a low wavenumber wave into two waves with higher wavenumber and half the original frequency) and induced diffusion (the scattering of a high-wavenumber high-frequency wave by a low-wavenumber low-frequency wave) fluxes

HWF consider the refraction of internal waves by the time varying velocity field of other internal waves. They used eikonal techniques and calculated the energy fluxes by means of Monte Carlo simulations of the ray equations.

Gregg concluded that his formulation that best-matched the observations was approximately one-third of the MM model, and twice the HWF model. However, once the discrepancy between the different employed GM forms and a more realistic portioning of the two mechanisms involved in MM is accounted for, all three models are approximately equal (see, Polzin et al., 1995; Polzin, 2004, for detailed discussion).

From a drifting ice camp in the eastern Arctic Ocean where the internal wave field was dominated by tides and high-frequency wavepackets, Wijesekera et al. (1993, referred to as W93) reported that their observations were best described by a strain-based estimator:

$$\varepsilon_{\text{W93}} = 7 \times 10^{-10} \frac{\langle N^2 \rangle}{N_0^2} \frac{\langle \zeta_z^4 \rangle_{10}}{\langle \zeta_z^4 \rangle_{\text{GM}}} \quad [\text{W kg}^{-1}]. \quad (5)$$

In this ad hoc scheme, G89's GM normalized shear variance is replaced by the strain variance.

Polzin et al. (1995, referred to as P95) tested different scalings including MM and HWF using a data set with a wide range in N , which also included observations from non-GM conditions. The dissipation, ε , was found to depend primarily upon N^2 and the spectral amplitude. The variability associated with the non-GM conditions were found to be primarily related to the frequency distribution of the internal wave field in the environment, which could be accounted for when inferred from shear-to-strain ratio. On the other hand, dissipation was found to be rather insensitive to the variations in the slope of the vertical wavenumber shear spectrum, and spectral asymmetry and inhomogeneity. Application of a frequency-based correction to the HWF model returned dissipation values consistent with observed estimates to within a factor of 2:

$$\varepsilon_{\text{P95}} = \varepsilon_0 \frac{\langle N^2 \rangle}{N_0^2} \hat{E}^2 \frac{\alpha}{\alpha_0} \frac{N}{f} \left\langle \left(\frac{\omega^2 - f^2}{N^2 - \omega^2} \right)^{1/2} \right\rangle \times L(f, N) \quad [\text{W kg}^{-1}]. \quad (6)$$

The last term is $L(f, N) = [f \cosh^{-1}(N/f)]/[f_{30} \cosh^{-1}(N_0/f_{30})]$ and is latitude dependant through f with f_{30} evaluated at 30°N . Here,

$\alpha = (R_\omega + 1)/R_\omega$ with a GM value of $\alpha_0 = 4/3$ and $\varepsilon_0 = 7.8 \times 10^{-10}$ is approximately the HWF value evaluated for canonical N_0 , E_{GM} and f_{30} . \hat{E} is the internal wave energy normalized by the GM level and can be expressed in terms of shear variance, shear spectral density or cutoff wavenumber. Under the hydrostatic assumption the term $N/f \langle (\omega^2 - f^2) / (N^2 - \omega^2)^{1/2} \rangle$ simplifies to $[2/(R_\omega - 1)]^{1/2}$. Eq. (6) can then be written as

$$\varepsilon_{P95} = \varepsilon_0 \frac{\langle N^2 \rangle}{N_0^2} \left(\frac{0.1}{k_c} \right)^2 \left(\frac{1 + 1/R_\omega}{4/3} \right) \left(\frac{2}{R_\omega - 1} \right)^{1/2} \times L(f, N) \text{ [W kg}^{-1}\text{]}, \quad (7)$$

where the term \hat{E} in Eq. (6) has been replaced by $(0.1/k_c)^2$, the squared ratio of the GM cutoff wavenumber (0.1 cpm) to the observed cutoff (k_c cpm) where k_c has been chosen such that the integrated shear spectrum equals $\sim 0.7N^2$ (see e.g., Gregg et al., 2003).

\hat{E} can equivalently be expressed in terms of the shear variance $\langle V_z^2 \rangle / \langle V_z^2 \rangle_{GM}$ (see, e.g., Naveira Garabato et al., 2004a, b). The terms including R_ω are corrections for the non-GM conditions and go to unity in a GM field ($R_\omega = 3$). Neglecting the latitude variability ($L = 1$) and further expressing \hat{E} in terms of 10-m shear variance, Eq. (7) approaches to ε_{G89} . More recently, Sun and Kunze (1999) extended the ray-tracing simulation of HWF and suggested an upper limit approximately reproducing Polzin et al. (1995) results, and a lower limit with turbulence production rates a factor of 4 smaller.

Finally, albeit not based on internal wave-wave interaction theory, Lass et al. (2003) reported that the averaged dissipation rate profile in the stratified part of the water column in the Baltic proper scaled as $\varepsilon_{L03} \propto (\text{KE} + \text{PE})N$ where the kinetic energy is $\text{KE} = (u^2 + v^2)/2$ and the potential energy is $\text{PE} = (\zeta^2 N^2)/2$. A scaling coefficient of 1×10^{-3} yielded best fit to their observations, indicating that about 0.1% of the internal wave energy was lost per local buoyancy period. In the following we will evaluate ε_{G89} , ε_{W93} , ε_{P95} (Eq. (7)) and ε_{L03} using our data set.

2.3. Site and recent work in Storfjorden

Storfjorden, located in the southeastern Svalbard Archipelago, is approximately 190 km long and 190 m deep at its maximum depth. It is enclosed by Spitsbergen to the west and north, by Barentsøya and Edgeøya to the east, the shallow bank

Storfjordbanken to the southeast and a 115-m deep sill at about 77°N in the south (Fig. 1). South of the sill is Storfjordrenna, which is separated from the main part of the Barents Sea by the shallow Svalbardbanken. Significant quantities of dense water originate in its recurrent polynya at the lee-side of Edgeøya and Barentsøya, which typically opens during northeasterly winds.

Ice and brine production in Storfjorden is most recently reported in Skogseth et al. (2004). Typically a volume flux of 0.06–0.07 Sv ($1 \text{ Sv} \equiv 10^6 \text{ m}^3 \text{ s}^{-1}$) of brine-enriched shelf water is produced when averaged over the freezing period (half that when averaged annually). The densest water masses spill towards deeper depressions, gradually fill up the basin to the sill level and overflow. The overflow can reach great depths depending primarily on its salinity anomaly. A more general description including the typical annual cycle of production and the resulting overflow together with the overflow dynamics are given in Skogseth et al. (2005a).

The mixing and spreading of the overflow during May 2001 were investigated by Fer et al. (2003) using velocity and CTD profiles in the outer part of Storfjordrenna. The net volume transport out of a section close to the sill was estimated to be 0.06 Sv, which nearly doubled by the furthest downstream section. Model results yield a transport of 0.11 Sv (Jungclauss et al., 1995), comparable to the field observations. Combined results from long-term time-series observations of currents and hydrography suggest that during fall and winter months near-bed currents and bottom stress can re-suspend sediment in response to strong flows by surface cooling and winds (Sternberg et al., 2001). Fer et al. (2004) inferred Thorpe scale-based estimates of mixing from conventional CTD profiles to show that the vertical diffusivity K_ρ was enhanced near the bottom (associated with the overflow plume), and decreased with the buoyancy frequency as $N^{-1.2 (\pm 0.3)}$.

3. Measurements

3.1. Instruments, data and data collection procedure

The microstructure data were collected by our MSS profiler, a loosely tethered free-fall instrument equipped with two airfoil probes (PNS98) aligned parallel to each other, a fast response conductivity (capillary type two electrode probe) and temperature (FP07), an acceleration sensor and conventional

CTD sensors for precision measurements. The sensors point downward when the instrument profiles vertically, and all sample at 1024 Hz to 16-bit resolution. An earlier version of the profiler is described by Prandke and Stips (1998), and results from a recent survey deploying a comparable version have been reported in Lass et al. (2003). The profiler is 1.4 m long, 106 mm in diameter, and weighs ~ 8 kg in air, hence easily handled by one person. The instrument is ballasted to free-fall at a typical fall speed of $0.6\text{--}0.7\text{ m s}^{-1}$ and is decoupled from operation-induced tension by paying out cable at sufficient speed to keep it slack.

The profiler is equipped with a sensor protection cage at the leading end. All profiles were within 10 m height above bottom (hab, hereafter), and in 24 out of 44 casts, the instrument landed at the bottom. The artifact of the protection cage is two significant narrow band peaks in the shear spectra, at ~ 24 Hz caused by von-Karman vortex shedding and at 44 Hz due to the cage's oscillations. With the mean fall speed of 0.65 m/s, the 24 Hz peak corresponds to a wavenumber of ~ 37 cpm. The wavenumber range chosen for the analysis is well below this peak (Section 3.2).

Observations were made during the first of a series of ProClim cruises, from R.V. *G.O. Sars* in Storfjorden, in September 2003. This was a multi-purpose cruise and the microstructure deployments were conducted between 7 September 10:30 and 9 September 16:00 UTC, interrupted by CTD stations and mooring deployment/recovery. In total eight stations were occupied, each for about 1 h duration, when typically five repeat casts were made (see Fig. 1 for positions). The mean time of occupation of each station is shown in Fig. 2 in relation to the cross-sill barotropic tidal current estimates at the sill (see Section 4). The profiler was dropped from the starboard side, repeatedly, while the vessel was drifting with the main engine and the thrusters switched off. Dissipation data in the upper 10 m are unreliable due to contamination of the ship's wake.⁵

Fine-scale velocity profiles were collected from a lowered-acoustic Doppler current profiler (LADCP) system mounted on the CTD frame. The hardware used comprised two RDI 307 kHz workhorse ADCPs (one looking upward and a second one looking downward) set to sample in bottom-track

mode at 0.5 s ping intervals at 5 m length vertical bins. The instruments were connected to each other in a master–slave mode and pinged simultaneously. Six of the eight stations had accompanying LADCP measurements, and data were used for examining the internal wave parameterizations and K_ρ –Richardson number ($Ri = N^2/V_z^2$) dependency (Section 5). Data from all casts were used for examining the K_ρ – N dependency and the Thorpe-scale analysis (Section 5).

3.2. Data reduction, processing and analysis

3.2.1. Small to microstructure

Full-scan (1024 Hz) data from all channels of the MSS profiler are edited for transmission errors and spikes and then averaged to 256 Hz to reduce noise. Time series are converted into vertical wavenumber space using a smooth fall-speed profile, invoking Taylor's frozen turbulence hypothesis (valid at the fall speeds reported here). The fall speed is derived from the time derivative of the (2-Hz low passed) pressure record. The dissipation rate of turbulent kinetic energy per unit mass, ε , is calculated using the isotropic relation $\varepsilon = 7.5\nu\langle u_z^2 \rangle$, where ν is the viscosity of seawater (here, it is approximated as a function of temperature and ranges within $1.55\text{--}1.9 \times 10^{-6} \text{ m}^2 \text{ s}^{-1}$ for the recorded range of temperatures -1.8 to 5°C), u_z is the shear of the horizontal velocity resolved at cm-scales. Shear wavenumber spectra are calculated using half overlapping 256-point Hanning windows (corresponds to 0.65-m windows for a nominal fall speed of 0.65 m s^{-1}). The shear variance is obtained by integrating the shear wavenumber spectrum between 2 cpm (a limitation due to the length of the profiler) and an upper cutoff number depending on the Kolmogorov wavenumber, $(\varepsilon/\nu^3)^{1/4}/2\pi$ cpm. The upper cutoff is determined by iteration, similar to that described in Moum et al. (1995), and is set to maximum 30 cpm (or 14 cpm when 2–14 cpm integrated $\varepsilon < 2 \times 10^{-8} \text{ W kg}^{-1}$). This range is not affected by the narrowband noise peaks. A fit to the universal shapes is avoided; however, a small correction (typically within a factor of 1.2 for $\varepsilon < 10^{-7} \text{ W kg}^{-1}$ and about a factor of 1.7 for $\varepsilon \sim 10^{-6} \text{ W kg}^{-1}$) is applied for the lost variance assuming the Nasmyth's form as tabulated in Oakey (1982). A further check is employed by comparing dissipation values from both probes, and anomalous data were discarded prior to averaging and gridding at 0.5 m resolution. The noise level

⁵The depth of the keel of the vessel is 7.5 m when the vessel-mounted ADCP is lowered.

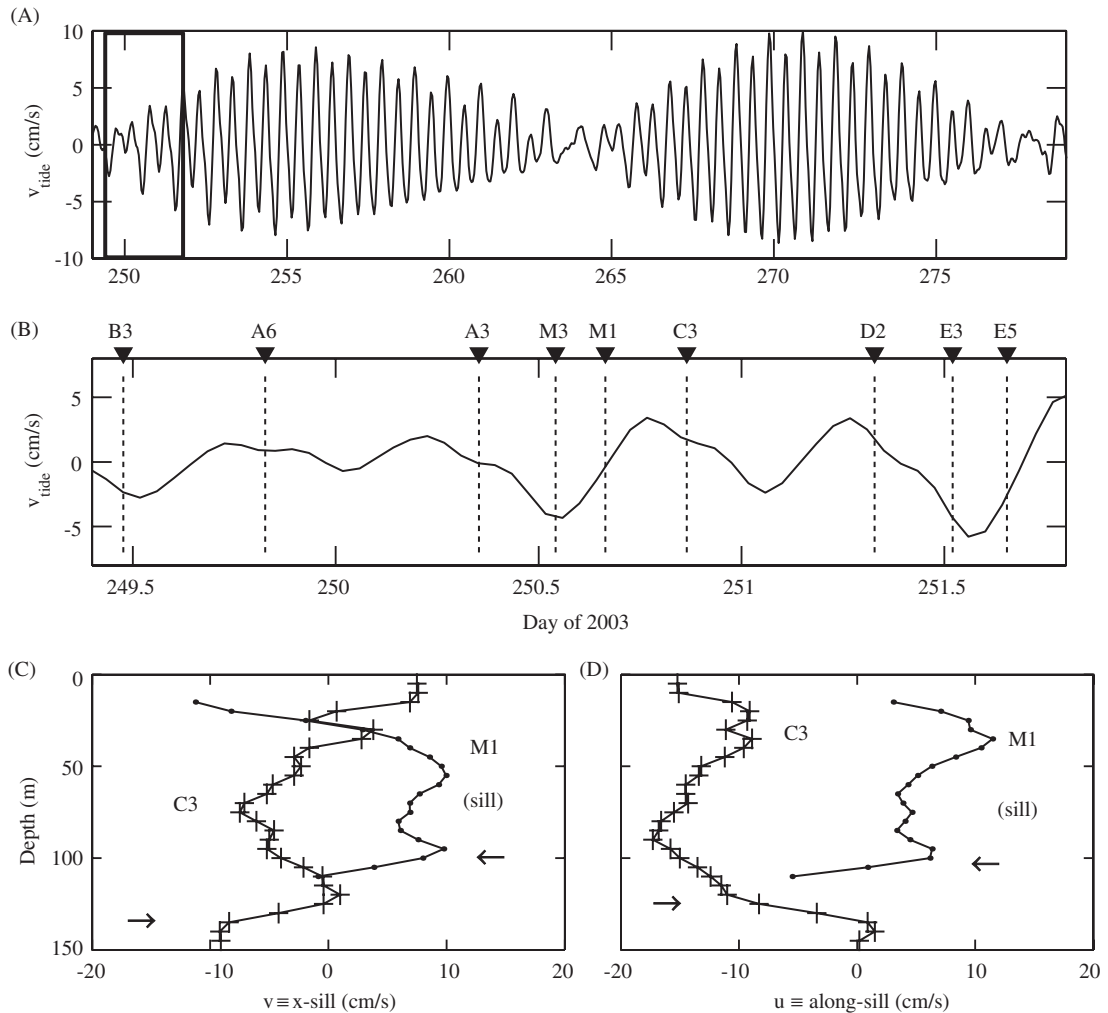


Fig. 2. Extract of time series of (A) the north component of the tidal current estimated from an upward looking ADCP moored at the sill and (B) the blow-up of the rectangle in (A) covering the shipborne observation period. Day 249.5 corresponds to 7 September 2003, 1200 UTC. Occupations of typically 1-h duration stations are indicated in (B). The sill is oriented approximately along east-west and the north (east) component is equivalent to the cross (along) sill component. The cross-sill (C) and along-sill (D) velocity profiles measured by the LADCP at stations M1 and C3 (separated by 6.3 h, approximately half the semidiurnal period). Arrows are at identical depths to that of Fig. 3A, showing the vertical extent of the dense water plume.

measured in quiet regions appears to be about $\sim 1\text{--}3 \times 10^{-9} \text{ W kg}^{-1}$. Minimum calculated values of ε from the two airfoil probes are 1.2×10^{-9} and $1.4 \times 10^{-9} \text{ W kg}^{-1}$, and over all 0.5-m ε values 1.3% were $< 5 \times 10^{-9}$ and 9.3% were between $(5\text{--}10) \times 10^{-9} \text{ W kg}^{-1}$. Because ε is directly proportional to the viscosity, our dissipation values will be a factor of 1.5–1.9 larger than those reported for relatively warmer waters (e.g., $\nu = 10^{-6} \text{ m}^2 \text{ s}^{-1}$ at 20°C). The typical “pseudo” dissipation rates, derived identically from spectral analysis of the acceleration sensor divided by the fall speed (Moum and Lueck, 1985), are $< 10^{-10} \text{ W kg}^{-1}$.

The vertical diffusivity for mass is approximated using $K_\rho = \Gamma \varepsilon / N^2$ (Osborn, 1980), where Γ is related to the mixing efficiency and typically $\Gamma = 0.2$ (Moum, 1996).

In the context of this work, data from the fast response thermistor and the conductivity sensor are only used to visually verify the enhanced turbulence patches. An independent estimate of vertical diffusivity (for heat) K_T (typically $\sim K_\rho$) using the Osborn–Cox model (Osborn and Cox, 1972) is not attempted due to the unknown response function and the lack of resolution of the thermistor.

Precision temperature and conductivity data are matched with a time-lag yielding the minimum salinity variance and conductivity data are filtered using an exponential recursive filter with the corresponding time constant (typically 0.2 s). CTD data are then averaged at 10-cm intervals prior to calculating spike-free salinity, S , potential temperature, θ , and σ_θ . Buoyancy frequency, $N(z)$, is calculated using the Thorpe-ordered density profiles (Thorpe, 1977), with density gradient obtained from the slope of linear fits to 20-m sliding boxcar windows. The 20-m scale is chosen to be consistent with the LADCP-derived shear in Ri calculations. Thorpe displacements are obtained from 10-cm averaged density profiles with a noise threshold for density of $2 \times 10^{-3} \text{ kg m}^{-3}$ determined after tests of Galbraith and Kelley (1996).

3.2.2. Fine structure

Nearly full-depth, covering 5 m from surface to ~ 5 m hab, 5-m vertically averaged profiles of horizontal velocity are computed by the inverse algorithm of Visbeck (2002) applied to the bottom-referenced LADCP velocity profiles. Profiles of isopycnal displacement, ζ , are calculated relative to the survey-averaged potential density profile. Depth of evenly spaced isopycnal surfaces (at 0.002 kg m^{-3} resolution) are computed via linear interpolation for each cast, and then averaged to yield the survey-averaged profile. Displacement of each isopycnal for each cast is calculated relative to its mean depth. Resulting displacement versus density profiles are converted to displacement versus 10-cm resolution depth profiles by linear

interpolation. The N profiles are averaged into 5-m depth bins to be consistent with the LADCP data. Depth mean velocity and linear fits to ζ with zero at the surface are subtracted to remove barotropic contributions (Kunze et al., 2002). Velocity spectra are obtained as the sum of clockwise (CW) and counterclockwise (CCW) components of the rotary spectra. Displacement spectra are calculated from 10-cm resolution displacement profiles. The shear and strain spectra are calculated by multiplying the velocity and displacement spectra by wavenumber squared.

We have limited our spectral analysis of fine structure to the 80-m (or more for relatively deep casts) portion of the profiles where N was approximately constant (within a factor of 2). Average values and variability of chosen parameters are listed in Table 1 for the analyzed depth portions of the stations. The 80-m minimum length was chosen to ensure an FFT length of 16 5-m samplings. The attenuation of the shear spectra due to range averaging of the LADCP is corrected by the response function described in Polzin et al. (2002). Shear spectra are normalized by the squared- N , averaged in the selected portion of the profile. Variances for shear and strain are calculated by integrating the associated spectra to a cutoff wavenumber where integrated shear variance equals $\sim 0.7N^2$. This cutoff was always less or equal to 0.05 cpm (20 m wavelength) after which the noise dominates for the shear data (shear noise, clearly distinguishable in Fig. 5 introduced later, increases with wavenumber when white noise is assumed for the velocity spectra). Individual as well as

Table 1

Average values of chosen parameters for selected depth portions (column 2) of the stations (column 1) where the buoyancy frequency, N (column 3, mean \pm one standard deviation) is approximately constant

Station	Depth range (m)	N ($\times 10^{-3} \text{ s}^{-1}$)	ε ($\times 10^{-8} \text{ W kg}^{-1}$)	K_ρ ($\times 10^{-4} \text{ m}^2 \text{ s}^{-1}$)	$\frac{\langle (v_z^2)^2 \rangle}{\langle v_z^2 \rangle^2}$	$\frac{\Phi_{\text{CW}}}{\Phi_{\text{CCW}}}$	R_ω
E3	50–170	4.2 ± 1.2	5.2 [4.1; 4.6; 5.2]	5.9	2.7	0.7	3
E5	50–210	3.4 ± 1.0	1.8 [1.7; 1.8; 1.9]	3.1	2.2	3.3	4.8
B3	25–105	5.9 ± 1.4	10.2 [6.8; 8.8; 11.6]	5.9	1.5	0.1	6.4
C3	45–125	5.5 ± 1.1	2.5 [2.4; 2.5; 2.6]	1.7	2.5	2.4	1.1
D2	40–120	5.0 ± 1.0	4.1 [3.0; 3.4; 3.9]	3.3	2.9	1.2	1.3
M1	25–105	7.3 ± 2.0	3.0 [2.7; 2.9; 3.1]	1.1	2.2	0.1	1.3

Fourth column is the dissipation rate arithmetic mean and lognormal statistics (Baker and Gibson, 1987) in brackets (95% lower confidence limit, maximum likelihood estimator; and 95% upper confidence limit). Fifth column is the diapycnal diffusivity. In the sixth column the ratio of the mean-shear-variance squared to the squared mean-shear-variance is given. Seventh column is the ratio of clockwise to counter-clockwise velocity variance at the lowest wavenumber 0.0125 cpm. Final column is the shear-to-strain ratio obtained by integrating the corresponding spectra between 0.0125 and 0.05 cpm.

ensemble-averaged velocity spectra (not shown) indicate that the noise is less than 2 cm s^{-1} in the rms sense. To be consistent, observed variances and the corresponding GM values are calculated at the same wavenumber bands.

When finite differencing is used (for full-depth application of G89 and L03, and Ri calculation), a 20-m interval is employed with 5-m moving window, hence we use 20-m shear variances in Eq. (4). A correction factor of 2.3, relative to the GM shear variance integrated to 0.05 cpm, is applied to account for 20-m finite differencing and 5-m range averaging of the LADCP (the correction applied by G89 for 10-m finite differenced expendable current meter data was 2.11).

4. Fine-scale and micro-scale characteristics

Before attempting to compare our observations with various models, we present chosen data to describe the context of mixing at the site and the data quality. The time of occupation of each station is shown in Fig. 2 with respect to the tidal current estimated from a bottom-mounted upward looking RDI ADCP (307 kHz workhorse) moored at the sill. The year-long time series (4-m vertical bins between 6–94 m hab at 111 m isobath) from this instrument is being analyzed for ongoing work and here it is only used to present the estimated barotropic tidal currents. Depth-averaged values of velocity from the LADCP casts near the sill and those at the same time from the ADCP moored at the sill agree within $\pm 2 \text{ cm s}^{-1}$. The stations were occupied during neap tides when typical cross-sill tidal component was $\pm 5 \text{ cm s}^{-1}$. The sill is oriented along east-west, thus the north (east) component can be considered as the cross-sill (along-sill) component, with positive values into the fjord. Velocity profiles from LADCP are shown for C3 ($\sim 15 \text{ km}$ downstream of the sill) M1 (sill), separated by $\sim 6.3 \text{ h}$ (approximately half the semi-diurnal or the local inertial period). The profiles roughly mirror each other in relation to the phase of the tide (note that the stations are 15 km apart) and the signature of the bottom-intensified plume can be identified (arrows in Fig. 2C and D are at the same depths as in Fig. 3A and mark the vertical extent of the plume). At the time of occupation of M1, the cross-sill component of the tidal velocity is ~ 0 , whereas the cross-sill component of LADCP-derived velocity at M1 reaches $\sim 10 \text{ cm s}^{-1}$ at mid-depth and contains non-tidal terms.

MSS-derived profiles averaged over the ensemble of casts at three representative stations (upstream of the sill, M3; at the sill, M1; and downstream of the sill, C3) are presented in Fig. 3. The water column is continuously stratified below the pycnocline located at 20–40 m. In Storfjordrenna, water denser than $\sigma_\theta > 27.95$ (at and downstream of the sill, marked by arrows in Fig. 3A) can be attributed to the dense-water plume of Storfjorden origin (Fer et al., 2003), clearly distinguishable as ~ 15 - and ~ 60 -m thick (including the interface at the top of the homogeneous layer) bottom layers at M1 and C3, respectively. Mixing is enhanced at the sill by an order of magnitude, associated with the overflow (Fig. 3A and B). An elevated level of dissipation is observed at the downstream station below the plume–ambient interface, whereas the diffusivity is large throughout the thickness of the plume, because of the weak stratification. Both at the sill and at the downstream stations the bottom values of K_ρ are $O(10^{-3}) \text{ m}^2 \text{ s}^{-1}$, i.e. two decades larger than typical open-ocean thermocline values or 10 times the value necessary to maintain the global overturning circulation (Munk, 1966). The so-called buoyancy Reynolds number (or index for activity of turbulence), $Re_\rho = \varepsilon/\nu N^2$ is typically greater than 200 (Fig. 3D), the threshold when the local isotropy is achieved (Yamazaki and Osborn, 1990). At all depths $Re_\rho > 20$, the approximate lower limit of “turbulence”, i.e. below which diffusivities of heat and salt are near molecular levels (Stillinger et al., 1983).⁶ Typically > 50 data points (n in Fig. 3D) are averaged in each 2-m bin for this illustration (about five half-overlapped ε estimates per shear sensor/per cast/per 2 m at $\sim 0.65 \text{ m s}^{-1}$ fall speed, but only about three are independent). Dissipation spectra from two portions of the profiles where ε differs by an order of magnitude are presented and contrasted to Nasmyth’s curve in Fig. 4. In this dynamically active system, the low values of ε are $O(10^{-8}) \text{ W kg}^{-1}$, at least a factor of 2 above the noise level of the instrument and approximately adhere to the Nasmyth’s curve in the resolved wavenumber range. For the portions of the data selected for analysis (Table 1), the arithmetic mean $\langle \varepsilon \rangle$ is within 20% of the estimator from lognormal statistics (Baker and Gibson, 1987) and we assume $\langle \varepsilon \rangle$ was adequately sampled to overcome intermittency.

⁶For the noise level $\varepsilon \sim 10^{-9} \text{ W kg}^{-1}$, $\nu = 1.7 \times 10^{-6} \text{ m}^2 \text{ s}^{-1}$ and $N = 5 \times 10^{-3} \text{ s}^{-1}$, $Re_\rho \sim 24$.

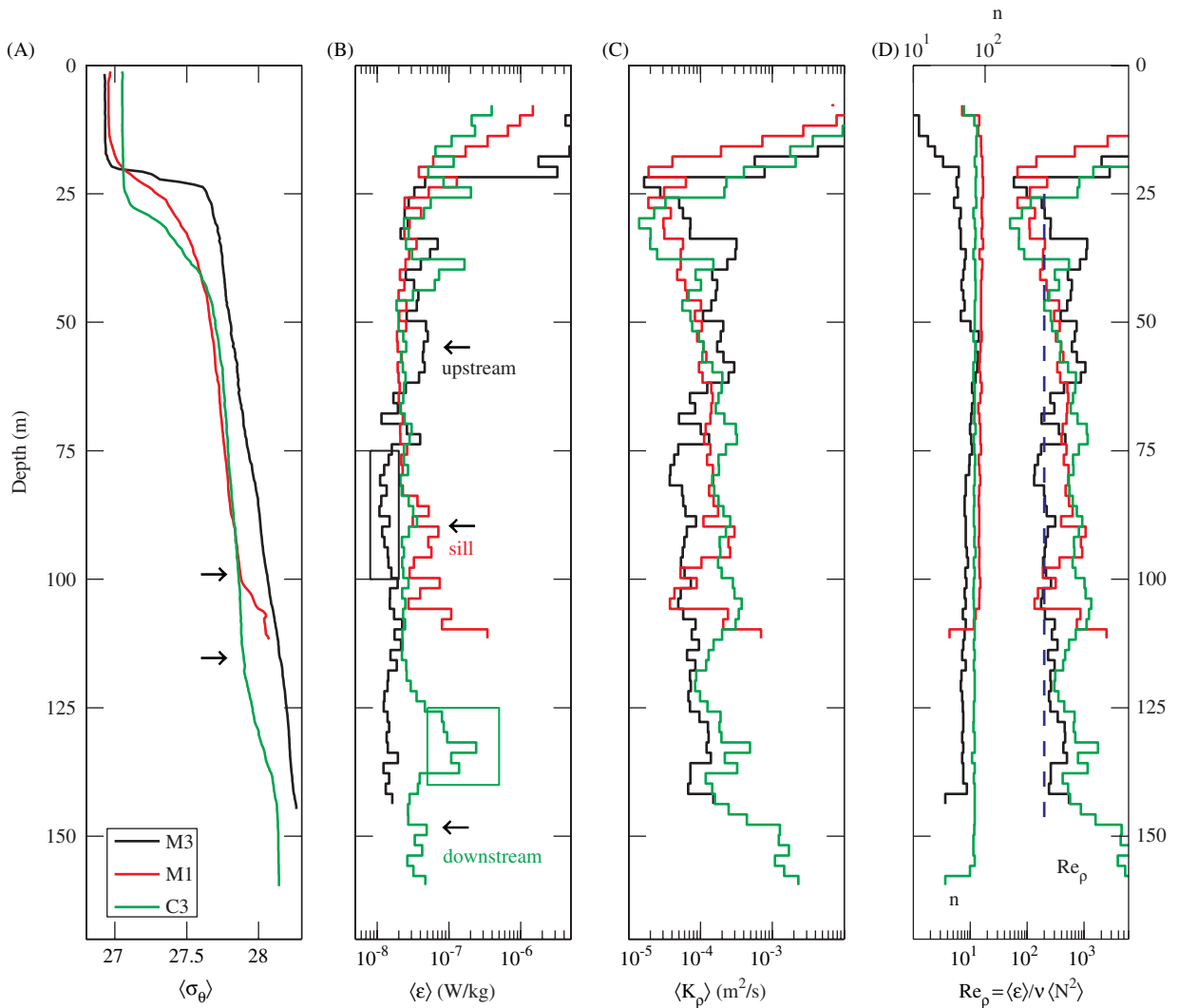


Fig. 3. Ensemble-averaged profiles of (A) σ_θ , (B) dissipation rate ε , (C) diapycnal diffusivity K_ρ , and (D) number of data points (n) in each 2-m bin and Re_ρ at the sill (M1), upstream of the sill (M3), and downstream of the sill (C3). Data presented in (B–D) are averaged into 2-m bins. Arrows in (A) show the approximate thickness of the dense plume. Boxes in (B) are the portions from which the dissipation spectra are shown in Fig. 4. Dashed line in (D) is $Re_\rho = 200$, the threshold when local isotropy is believed to be achieved.

Survey-averaged spectra of strain and N -normalized shear are contrasted to the GM76 model (Fig. 5). There is one LADCP-derived shear spectrum at each station (eight 80-m segments are averaged: 50% overlapped two segments in E3, two segments in E5, and one segment each in other profiles) and confidence intervals are shown for 16 degrees of freedom. Strain spectra are derived from 10-cm averaged MSS–CTD data from typically five repeat casts at each station. Resulting spectra are then band-averaged to identical wavenumbers of the shear spectrum for $k_z \leq 0.1$ and at $\Delta \log_{10}(k_z) = 0.1$ cpm intervals for larger wavenumbers. The

confidence intervals are therefore very tight (not shown). Both the shear and strain spectra are elevated above the GM76 levels. At high wavenumbers, strain spectra falls off comparable to the k_z^{-1} dependence. The cutoff wavenumber where the normalized shear variance equals 0.7 is 0.05 cpm, half that of GM76. Inverse Ri ($\equiv Fr^2$) is unity at 0.0875 cpm (~ 11 m), but this is probably slightly contaminated by the LADCP noise. The lowest two wavenumber bands suggest a nearly “white” average shear spectrum in agreement with GM76, before a sharp roll-off not inconsistent with the -1 roll-off of GM76. The roll-off in GM76 is believed to be

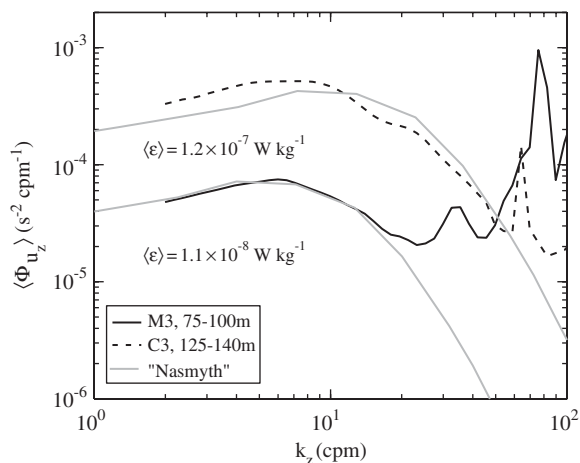


Fig. 4. Ensemble-averaged shear wavenumber spectra and the corresponding Nasmyth's spectra from two portions where ϵ vary by an order of magnitude. The systematic deviations of the shear at large wavenumbers do not affect our results because spectra are integrated up to a maximum cutoff wavenumber set to 30 cpm (or 14 cpm for $\epsilon < 2 \times 10^{-8} \text{ W kg}^{-1}$). The unresolved shear variance was corrected for assuming the Nasmyth's universal shape of the spectrum.

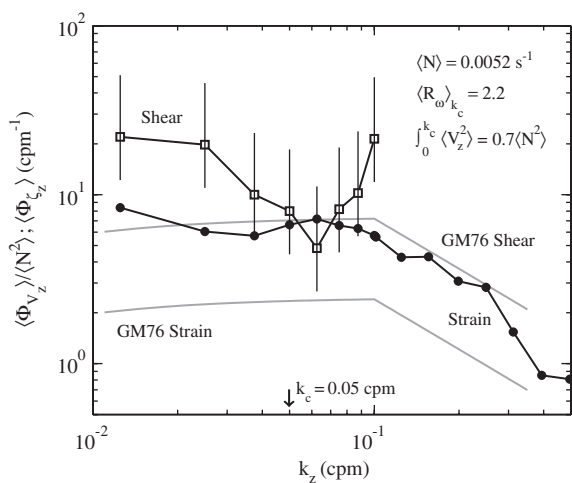


Fig. 5. Survey-averaged (over stations listed in Table 1) vertical wavenumber spectra of strain Φ_{ϵ_z} (dots) and N -normalized shear Φ_{V_z} (squares). Corresponding GM76 spectra also are shown. Error bars are 95% confidence intervals for shear (16 degrees of freedom). Due to several repeats at each station and 10-cm sampling interval of MSS-CTD confidence intervals (not shown) are not distinguishable from the observed strain spectrum. Average buoyancy frequency, N , shear-strain ratio, R_{ω} , and shear variance, both integrated to the cutoff wavenumber $k_c = 0.05 \text{ cpm}$ (arrow) are indicated. R_{ω} is given for the average spectra and is different from the average over individual station estimates equal to 3 (2.3 excluding B3, Table 1).

caused by strong nonlinear interactions, however because of the undersampling in shear and the lack of resolution in wavenumber space we cannot confidently argue on the spectral slope and the cutoff wavenumber for roll-off.

The shear-to-strain ratio, R_{ω} is about 2.2, less than but comparable to the GM value of 3, when derived from survey-averaged spectra (Fig. 5). The values derived from station-averaged spectra vary within 1–7 (Table 1, last column). Typical mid-latitude values are 3–5, comparable to R_{ω} for semi-diurnal frequency, M_2 . Here we are poleward of the critical latitude (74.5°) for M_2 and its effect on the dynamics is not clear. According to the linear theory, M_2 internal tides cannot propagate freely poleward of this latitude. However, existence of negative background vorticity can allow M_2 internal tide propagation even north of the critical latitude by effectively reducing the local inertial frequency (Kunze, 1985). Semi-diurnal baroclinic oscillations north of the critical latitude were observed during the Barents Sea Polar Front experiment (Kozubskaya et al., 1999), and their existence could be explained by changes in the effective inertial frequency, as well as with the manifestation of nonlinear effects (Vlasenko et al., 2003). A characteristic frequency of an internal wave derived from the maximum observed value of R_{ω} is $1.17f$ whereas low values at stations M1 and D2 are comparable with the M_4 frequency.

For near-inertial frequency internal waves, direction of energy propagation can be inferred from the sense of rotation with depth of the CW and CCW velocity or shear variance. In the Northern Hemisphere near-inertial motions with downward group velocity have CW rotation. Therefore an excess of CW (CCW) variance is often interpreted as downward (upward) energy propagation and the opposite is true for the phase propagation (Leaman and Sanford, 1975). The ratio Φ_{CW}/Φ_{CCW} around unity indicates vertical symmetry in the sense that the upward and downward propagating energies are comparable (note that GM76 assumes vertical symmetry; however dissipation is reported to be relatively insensitive to the departures from symmetry; Polzin et al., 1995). Values of $\Phi_{CW}/\Phi_{CCW} < 1$ are typically interpreted as evidence for generation of near-inertial frequency internal waves (e.g., M_2 internal tides) near a topographic feature, because near the generation site internal waves will have upward energy propagation. In our dataset, average Φ_{CW}/Φ_{CCW} is 1.3 at the largest resolved wavelength

of 80 m, suggesting vertical symmetry (at smaller scales all spectra are typically symmetric regardless of the behavior at large scales). At both occupations of the sill station (B3 & M1), this ratio is consistently $\ll 1$, suggesting upward energy propagation of internal waves possibly generated at the sill. This can be fortuitous and inconclusive due to undersampling. However, it is worth mentioning that this ratio is > 1 at C3, 15 km away from the sill, which is consistent with the argument that, if the generation is of M_2 internal tides, they cannot propagate freely long distances at this latitude and will dissipate locally (also note that dissipation and R_ω is largest at B3). Another possible explanation for the change in Φ_{CW}/Φ_{CCW} ratio is that if internal tides generated at the sill can propagate far enough, after surface reflection away from the sill they may be seen as downward propagating waves.

5. Results and discussion

5.1. Internal wave models

Observed values of ε and those derived from different models are contrasted in Fig. 6 for each portion described in Table 1. Among the internal wave–wave interaction models, the shear–strain model of Polzin et al. (1995) predicts the observed ε fairly well, with modeled to observed ratio scatter between 0.1–2 and 0.83 on the average. This model accounts for the non-GM properties of the wave field; however, the scatter suggests that other factors other than wave–wave interactions can play a role in the transfer of energy to smaller scales. The relatively large deviations from the observations can be partly due to the fine-scale shear undersampling and the inherent noise in LADCP data. The transfer function employed to the shear spectra is that for an ideally lowered ADCP (no tilt, rotation or beam separation due to lowering) for horizontally uniform currents (Polzin et al., 2002). Ignorance of transfer functions associated with these processes will bias the fine-scale shear low, which in turn will predict lower dissipation rates. Furthermore, when inferring eddy diffusivities, it is preferable to use larger bins for averaging velocity data from LADCP, e.g. inferences from 50-m variances of 20-m averaged profiles compared well with expendable current meter inferences in Polzin et al. (2002). Due to the shallow water depth we force the applicable limits of LADCP data and likely bias the estimates. This parameterization underestimated

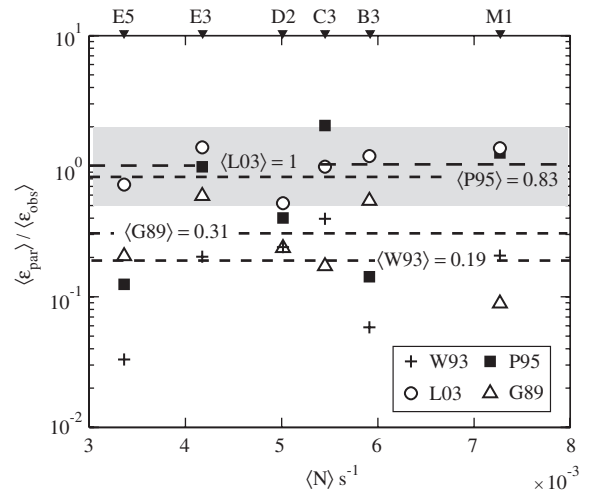


Fig. 6. The ratio of parameterized (ε_{par}) to observed dissipation (ε_{obs}) derived for each station (Table 1) as a function of the average buoyancy frequency, N , of the analyzed depth range chosen where N is nearly constant. Averages over the six stations are shown by dashed lines and the corresponding values. The stations are indicated on top at the corresponding N . The gray band is the factor of two range of agreement between model and observations.

the dissipation observations by a factor of 30 in Monterey Submarine Canyon (Kunze et al., 2002) where other processes than wave–wave interactions (e.g., interactions with topography, internal bores and solitary waves) are at play. Such processes can be expected to occur in the Storfjorden-sill system, but they are not resolved by our data set. Nevertheless the agreement, on the average, between the observations and the Polzin et al. (1995) model is encouraging and suggests that both shear and strain are important in determining the mixing in Storfjorden.

The 20-m shear variance (Gregg, 1989) and the strain variance (Wijesekera et al., 1993) alone appear to be a poor proxy, and underestimate the observations by a factor of 0.31 and 0.19, respectively. The G89 model actually comprises $\langle V_z^4 \rangle$ but in practice uses $\langle (V_z^2)^2 \rangle / \langle V_z^2 \rangle^2 = 2$, assuming Gaussian statistics. This ratio is listed in Table 1 and scatters in the range 1.5–2.9 with a mean value of 2.3 in our data set. The best fit of Lass et al. (2003) scaling suggests that 5×10^{-3} times the total energy is dissipated per buoyancy period, i.e. 5 times that observed in the Baltic proper. The scatter is within a factor 2, the typical uncertainty of dissipation measurements. The potential consequences of the vertical resolution, undersampling and analysis methods are further discussed in Section 5.5.

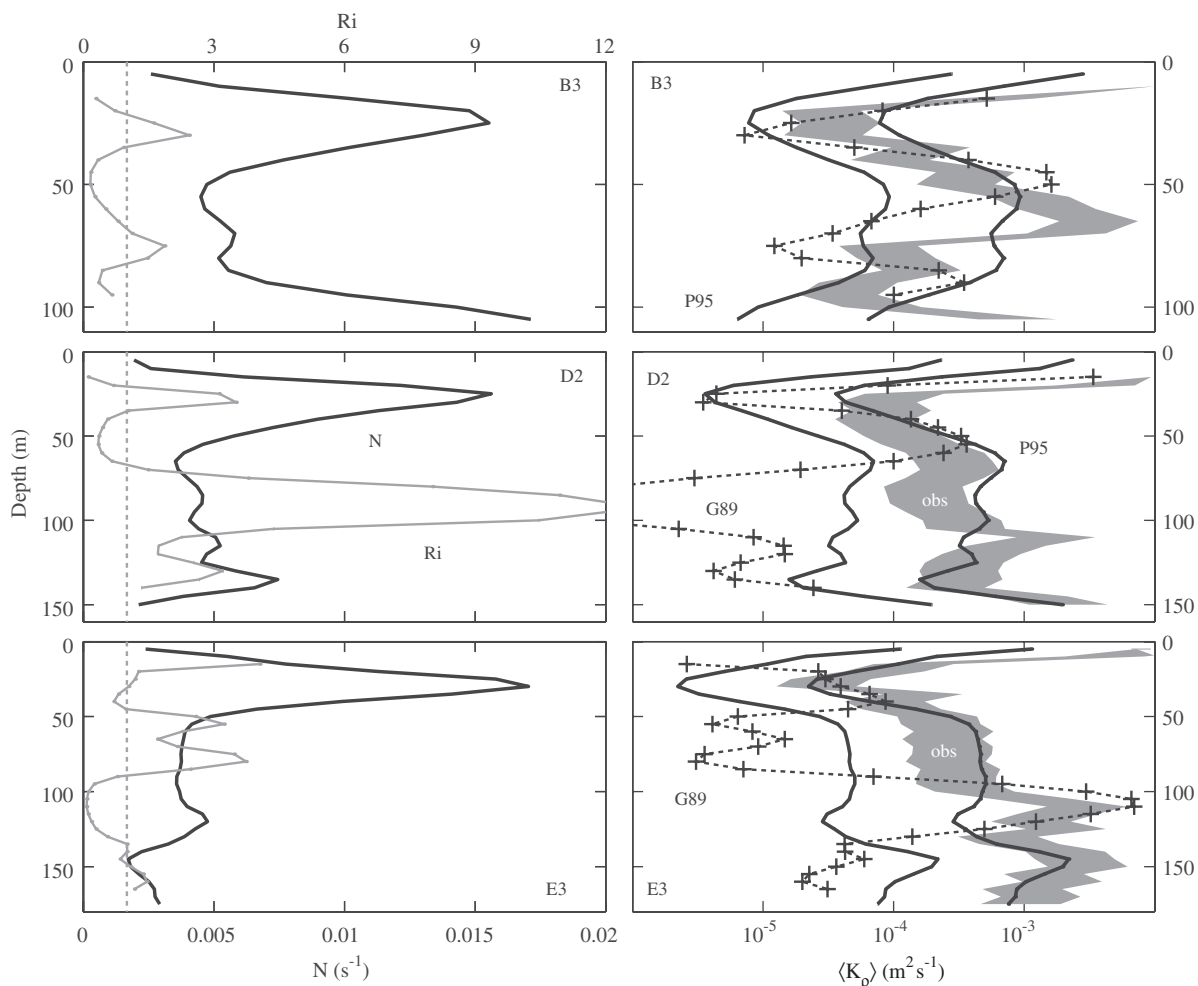


Fig. 7. Profiles of (left column) buoyancy frequency (N , black), Richardson number (Ri , gray), (right column) observed and inferred vertical diffusivity, K_p . Three chosen stations (upper panels, B3; middle panels, D2; and lower panels, E3) are shown. The observed K_p profile (gray band) is shown for a factor of 2 of the station average. 20-m finite differenced shear is used for G89. The P95 profiles are derived using $k_c = 0.05$ cpm and $R_\omega = 1.1$ for the upper limit for K_p and $R_\omega = 5$ for the lower limit for K_p .

In application of the internal wave models, the canonical parameters of the GM model are employed without any adjustment. Particularly, the stratification scale depth b , which plays a large role in the GM spectral density, is likely much less than 1300 m at the measurement site. Depth-averaged horizontal kinetic energy density in the internal wave continuum⁷ is $6 \times 10^{-4} \text{ J kg}^{-1}$. This is 0.2 times the canonical GM value of $E_{GM}(N_0 b)^2 \sim 2.9 \times 10^{-3} \text{ J kg}^{-1}$. Following the example procedure in

Section 4c of Levine (2002), an estimate of b can be made for the observation site. The integral of survey-averaged $N(z)$ (Fig. 8A) is $\sim 1 \text{ m s}^{-1}$ and provides an estimate for the product $N_0 b$, then using $N_0 = 5.24 \times 10^{-3} \text{ s}^{-1}$, $b \sim 190 \text{ m}$, significantly less than the canonical value, as expected. The measured non-dimensional energy is $6 \times 10^{-4} / (N_0 b)^2 \sim 6 \times 10^{-4}$, i.e. ~ 9.5 times E_{GM} . The shear variance obtained by integrating the GM76 shear spectrum with modified parameters ($b = 190 \text{ m}$, $E_{GM} = 6 \times 10^{-4}$, but same j_*) to 0.1 cpm is found to be within 5% of the canonical GM76 shear variance. This minor deviation is within uncertainties of any set of measurements presented in this work and we therefore chose not to alter the GM76 canonical parameters.

⁷It is computed by integrating (between $f-3$ cph) the depth-averaged horizontal baroclinic kinetic energy spectrum measured by the ADCP moored at the sill. Baroclinic velocity is estimated by subtracting instantaneous depth mean velocity from each bin at all times.

The profiles of stratification, Ri , and observed and inferred (Gregg, 1989; Polzin et al., 1995) diffusivities for three stations with increasing distance from the sill (B3 at the sill, D2, and E3) are shown in Fig. 7. Because the G89 model is derived using 20-m moving-window first-differenced shear variances, the K_ρ -depth profile can be constructed. The Polzin et al. (1995) model, on the other hand, employs a cutoff wavenumber and R_ω (Eq. (7)) derived from the shear and strain spectra (i.e., only mean values can be estimated from long-

enough records, here 80 m, that allow for spectral calculation). Nevertheless, we can estimate a range of survey-mean ε_{p95} (from Eq. (7) using the survey mean $N = 5.2 \times 10^{-3} \text{ s}^{-1}$ below the pycnocline and above the plume, $k_c = 0.05 \text{ cpm}$ (Fig. 5), and a typical range of $R_\omega = 1.1$ to 5), and apply Osborn's model using station-mean full depth N -profile to obtain a range of K_ρ profiles. The high K_ρ range of P95 (using $R_\omega = 1.1$) approximates the depth variability of diffusivity fairly well, but cannot capture some enhanced mixing events, e.g., at

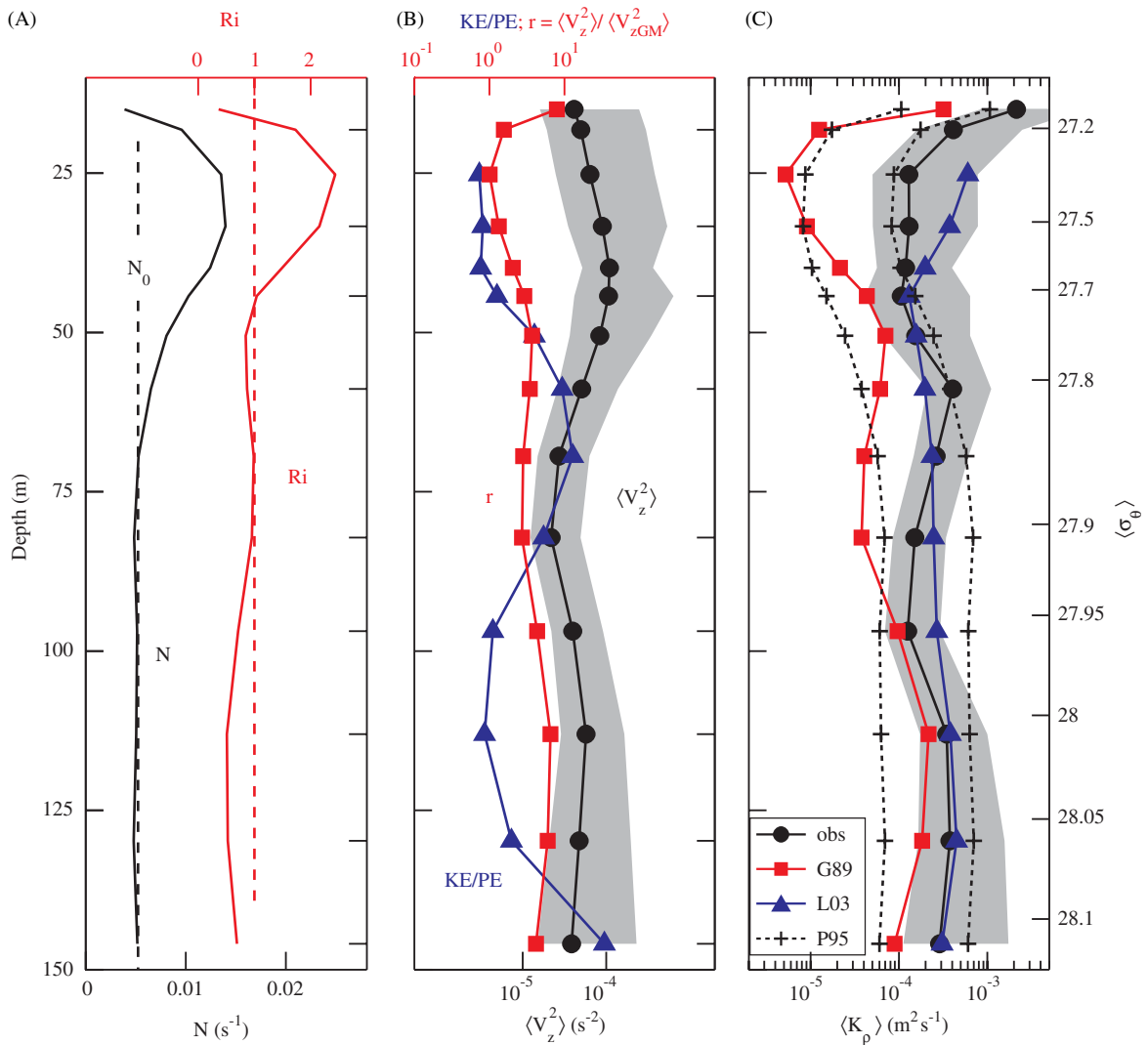


Fig. 8. Isopycnally averaged profiles of (A) N and Richardson number, Ri ; (B) observed shear variance V_z^2 , its ratio to GM shear variance (r), and kinetic energy to potential energy ratio (KE/PE); (C) observed diapycnal diffusivity K_ρ , and that parameterized by G89, L03, and P95. The P95 model is applied using $k_c = 0.05 \text{ cpm}$ and $R_\omega = 1.1$ for the upper limit of K_ρ and $R_\omega = 5$ for the lower limit of K_ρ . Data from all profiles at all LADCP stations (Table 1) are averaged into σ_θ bins and plotted with respect to the average depth within each σ_θ bin. The corresponding σ_θ profile is given by the ticks on the right vertical axis. 95% confidence intervals (gray envelopes in B and C) are derived from the number of samples in each bin. Dashed lines in (A) are $Ri = 1$ and the canonical N_0 .

mid-depth and bottom at B3 and at ~ 100 m at E3. Low Ri related mixing events (B3 at ~ 50 m; E3 at ~ 100 m) are successfully estimated by G89; however, undersampling (see Section 5.5) prevents to decide that one model is significantly better than the other.

The survey-averaged profiles are shown in Fig. 8. In this representation, isopycnally averaged values from all profiles with LADCP data are used and plotted against the average depth of chosen σ_θ bins. The P95, G89 and L03 scalings are applied to the whole water column and presented in terms of inferred diffusivities (Fig. 8C). A range of K_ρ profiles are estimated for P95 as explained above, but employing the survey mean N (Fig. 8A) in Osborn's relation. Stratification is close to N_0 and the 20-m Ri is around unity below the pycnocline. There is an excess of potential energy in the upper 50-m ($\sigma_\theta < 27.75$) but the average KE/PE is 4.6 for values of σ_θ between 27.7–28.05, the typical σ_θ range where spectral calculation of R_ω is conducted. Shear variance is about 3.6 times the GM level, on the average. Over the whole water column, inferred diffusivities using L03 typically fall within 95% confidence intervals of the observations. The success of L03 depends on being tuned with a constant of 5×10^{-3} .

Polzin et al. (1996) examined the question of whether elevated shears in frontal systems imply the same degree of enhanced mixing that would be inferred from G89 and P95 relations, essentially for a region of zero mean flow. They concluded that the wave–wave interaction based models should result in an accurate prediction of ε despite the presence of mean shear, particularly if background $Ri > 20$. Here, when inferred from the N -normalized shear spectra, at the lowest resolved 80-m wavelength $Ri = 3.6$ with 95% confidence intervals [2; 8.5]. The larger-scale Ri can be larger when the whole water column is considered, including the strongly stratified pycnocline. Geostrophic shear associated with the overflow and the Atlantic water circulation is comparable. It is likely that a representative background Ri is significantly less than 20, the threshold suggested by Polzin et al. (1996), such that we might expect some deviations from the wave–wave interaction models.

5.2. Diffusivity and stratification

The range of buoyancy frequency, N and K_ρ covered by our observations is 0.5–12 cph and

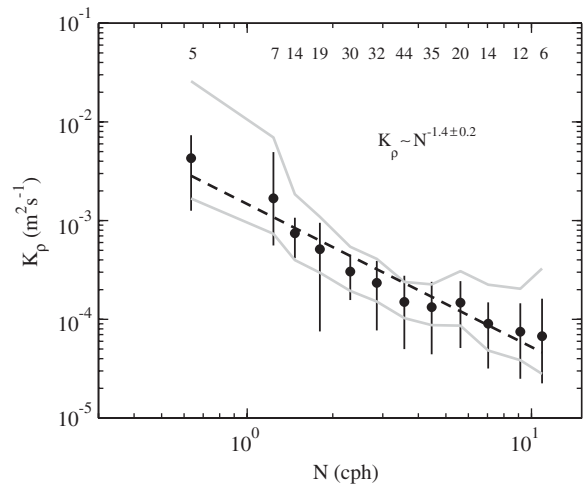


Fig. 9. Variation of K_ρ by buoyancy frequency, N . Data are averaged into $10 \log_{10}(N)$ -bins of equal size between 1 and 10 cph. All the values above and below this range are shown at their corresponding mean values. Error bars are one standard deviation and gray-envelope is 95% confidence interval derived over the number of data points in each bin (indicated on top). Dashed line shows -1.4 dependence obtained by the best fit in least-squares sense (95% confidence interval of the exponent is ± 0.2).

2×10^{-5} – $8 \times 10^{-3} \text{ m}^2 \text{ s}^{-1}$, respectively, and allows for an examination of K_ρ – N dependency. For a constant internal wave energy state, the wave–wave interaction mechanisms yield $\varepsilon \propto N^2$ scaling (G89, P95), which corresponds to K_ρ independent of N using Osborn's model. The best fit to the observations gives a power law $K_\rho \propto N^{-1.4}$ with 95% confidence interval of the exponent ± 0.2 (Fig. 9). Previous observations at the site resulted in decay of diffusivity by stratification with power not significantly different than -1 , when inferred from Thorpe scale analysis of CTD profiles (Fer et al., 2004). An N -scaling with power within -1 and -1.5 appears to be a robust feature of mixing in Storfjorden. This power law is very close to the $K_\rho \propto N^{-1}$ dependence consistently found for a variety of geophysical systems using various methods as compiled by Gargett (1984) and, in particular, to the best fits $K_\rho \propto N^{-1.2}$ in two different sillfjords derived from budget methods (the least model-dependant means of estimating K_ρ).

The average N for the portions of the profiles analyzed for wave–wave interaction models cover a range of 2–5 cph (Table 1). The discrepancy between observed and inferred diffusivities at and above the pycnocline (Fig. 8C) can be partly attributed to the N -dependency inherent in the data. The

scaling tested in L03 ($\epsilon \propto N$; $K_\rho \propto N^{-1}$) is based on Stigebrandt (1987) and better captures the observations in the upper 50 m. This power law is appropriate for breaking of narrow band internal waves (Gargett and Holloway, 1984) as well as for processes in lakes and fjords that are mixed by strong turbulent processes and localized instability of large-scale motions (D’Asaro and Lien, 2000).

5.3. Diffusivity and Richardson number

Because of their simplicity to implement on numerical models $K_\rho(Ri)$ relations are typically sought, among which that suggested by Pacanowski and Philander (1981, PP81) is widely used. The parameterization of vertical mixing given in PP81 is

$$K_m = \frac{5.5 \times 10^{-3}}{(1 + 5Ri)^2} + K_{m0} [\text{m}^2 \text{s}^{-1}], \quad (8)$$

$$K_\rho = \frac{K_m}{1 + 5Ri} + K_{\rho0} [\text{m}^2 \text{s}^{-1}], \quad (9)$$

where K_m is the vertical eddy viscosity, and $K_{m0} = 10^{-4} \text{m}^2 \text{s}^{-1}$ and $K_{\rho0} = 10^{-5} \text{m}^2 \text{s}^{-1}$ are the “background” values for eddy viscosity and eddy diffusivity, respectively. The PP81 model is a parameterization for a mean-sheared flow (the equatorial undercurrent), and background viscosity and diffusivity are above molecular values to account for the unresolved processes that cause mixing. We apply the model using full resolution (5-m) Ri to 158 $Ri-K_\rho$ pairs (the trend and conclusion is comparable for 20-m Ri , not shown). This model approximately captures the $Ri < Ri_c$ portion of our K_ρ observations and significantly underestimates K_ρ for larger Ri (Fig. 10, dashed red curve).

In order to provide a means of parameterization in the PP81 form for Storfjorden we chose to alter K_{m0} and $K_{\rho0}$. We did not measure eddy viscosity, K_m , but in order to preserve the PP81-type formulation (Eq. (9), $K_\rho \propto K_m$) we retain the K_m dependence in K_ρ . A satisfactory fit is obtained by simply elevating the background values to $K_{m0} = 1.3 \times 10^{-3} \text{m}^2 \text{s}^{-1}$ and $K_{\rho0} = 1.3 \times 10^{-4} \text{m}^2 \text{s}^{-1}$ (Fig. 10, solid red curve). This imposes a background turbulent Prandtl number (K_m/K_ρ) of 10. Using measurements of both shear and temperature microstructure and shipborne ADCP shear in a coastal system, Oakey and Greenan (2004) reported $K_m/K_T \sim 5Ri$ for Ri between 1 and 4.5. Assuming that the eddy diffusivity for heat $K_T \sim K_\rho$, a Prandtl number of 5–20 can be expected for our

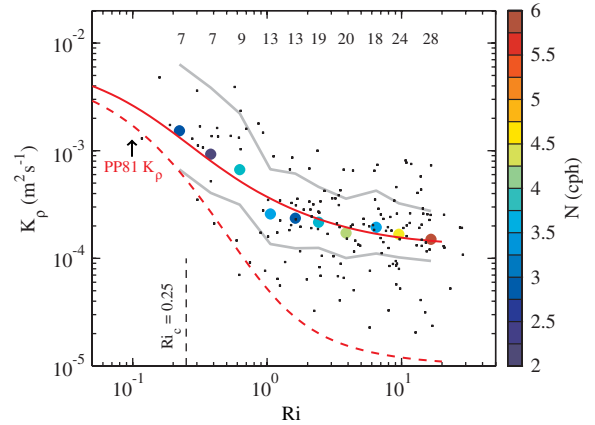


Fig. 10. Variation of K_ρ by 5-m Richardson number, Ri . All $Ri-K_\rho$ pairs (dots, 158 in total) and data averaged into equal $\log_{10}(Ri)$ bins are shown. The averaged data are color-coded for the buoyancy frequency, N . Gray-envelope is 95% confidence interval derived over the number of data points in each bin (indicated on top). Dashed vertical line is the critical $Ri = 0.25$. Widely used PP81 relation (Eq. (9)) is shown for eddy diffusivity with PP81 background values (dashed red curve) and with background values for eddy viscosity and diffusivity multiplied by a factor of 13 (solid red curve).

measurements. With the present data set, we cannot justify nor explain the need to raise the background (high Ri) diffusivity and viscosity, which should approach to their molecular values if both Ri and eddy diffusivity were fully resolved. This result should be regarded with caution and may be biased by the noise level in the MSS system and/or significant shear at small scales unresolved by the LADCP.

5.4. Thorpe scale and Ozmidov scale

Finally we examine the relation between the Thorpe scale, L_T (Thorpe, 1977), and the Ozmidov scale, $L_O = (\epsilon N^{-3})^{1/2}$. This relation is not probably useful for modeling purposes; nevertheless, is helpful to estimate mixing, at least that associated with patches of high turbulent activity, from carefully conducted and analyzed conventional CTD measurements resolved at 10–100 cm scale. Far from the surface in wind-forced mixing layers and in the seasonal thermocline Dillon (1982) reported $\langle L_T/L_O \rangle = 1.25$.

Vertical displacements are calculated to achieve monotonically sorted profiles using full-depth, 10-cm resolution station-mean density profiles. The Thorpe scale is computed as the rms of the

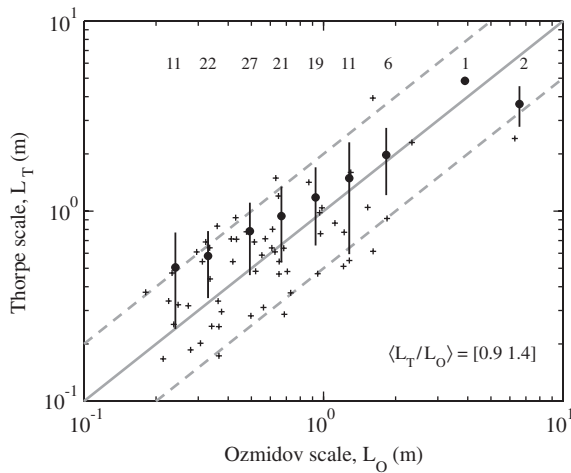


Fig. 11. Thorpe scale, L_T , versus Ozmidov scale, $L_O = (\epsilon N^{-3})^{1/2}$. The calculation is conducted over 5-m intervals (presented as averages in $\log_{10}(L_O)$ bins of equal size, dots with error bars) as well as over discrete overturn patches (presented for all 58 overturns, crosses). Error bars are one standard deviation over the number of 5-m derived data points in each bin (indicated on top). Diagonal lines cover a factor of two agreement. The 95% confidence limits of the mean ratio $\langle L_T/L_O \rangle = [0.9 \ 1.4]$ is derived over 1200 bootstrap samples.

displacements over (1) 5-m intervals (to be consistent with the fine-structure analysis) and (2) discrete patches of detected overturns (best method of comparing Thorpe-inferred and measured dissipation). The noise threshold for density and the significance of an overturn patch are determined after tests of Galbraith and Kelley (1996). In total 58 overturns are detected (crosses in Fig. 11). When comparing with Ozmidov scale, N and ϵ are averaged over 5 m for (1) and over the vertical span of the overturns for (2). The L_T and L_O comparison is shown for ensemble averages in $\log_{10}(L_O)$ bins for (1) (Fig. 11, dots with error bars) and for all individual overturns for (2) (Fig. 11, crosses). In our data set L_T and L_O scatter within a factor of 2 and the 95% bootstrap confidence limits on $\langle L_T/L_O \rangle$ is [0.9;1.4].

5.5. Caveats

Mixing models based on the internal-wave field assume shear and strain variances that are averaged over the dominant periodicity of the wave field. In this study, each station is occupied typically for 1 h and at varying phases of the semi-diurnal cycle. The fine-scale data (shear and strain) are undersampled both spatially and temporally, thus the background

and internal wave components of the flow field cannot be confidently separated. The corresponding variances are possibly not adequately represented nor averaged in the analysis. The parameterizations (G89, W93 and P95) are sensitive to the shear and strain variances and dissipation scales as the second power of the corresponding variance. In a previous attempt, when strain was calculated using displacements from the station-mean isopycnals (instead of the survey-mean), W93 model heavily underestimated the observations, because most of the strain variance is at lower frequencies. The strain variances are also questionable when derived relative to survey-averaged displacements in this anisotropic environment with significant hydrographic differences between stations (Fig. 3A). The validity of the strain-based estimator (in this environment) and also the P95 model (to which strain contributes through R_{ω}) can be better evaluated with proper sampling. Furthermore, due to averaging interval of LADCP and the significant noise at scales less than 20 m, we had to set the integration limit for the vertical wavenumber spectra to 0.05 cpm. This constrains the Richardson number distribution, R_{ω} , as well as the vertical wavenumber effective bandwidth, j_* . The reader is referred to Wijesekera et al. (1993) for a thorough discussion of difficulties in estimating model parameters and to Gregg and Kunze (1991) for a discussion of the effects of limited bandwidth. It also should be noted that the microstructure and fine-scale shear measurements are not simultaneous. The LADCP was deployed either before or after (but typically completed within 30 min) the batch of MSS profiles.

6. Summary and concluding remarks

We presented the first direct measurements of turbulence in Storfjorden, in September 2003, during conditions of weak overflow. Dissipation and diffusivity profiles at and downstream of the sill showed elevated levels of mixing within the plume and at the plume–ambient interface. This was also true for survey-averaged profiles, averaged isopycnally. The diffusivity was found to decay with stratification as $N^{-1.4(\pm 0.2)}$. The observations are in agreement with and confirm the indirect inferences reported for August 2002 (Fer et al., 2004).

There is some evidence, but not sufficient to conclude, that the sill might be generating internal waves which dissipate locally. There is an excess of CCW low-wavenumber shear variance at the sill,

indicative of upward propagating near-inertial internal wave energy, which disappears within 15 km off the sill. At two occupations of the sill station, a characteristic frequency derived from the shear-to-strain ratio alternates between $1.17f$ and approximately M_4 .

In Storfjorden, survey-averaged spectral levels of both shear and strain were larger than GM76. Vertical structure was rather symmetric, i.e. upward and downward propagating energies were similar, and the shear–strain ratio was slightly less than the GM in the stratified interior. After applying different models and scalings we conclude the following. Background dissipation in the interior can be parameterized by the shear and strain model of P95, based on internal wave–wave interaction arguments. Diffusivity can be inferred using P95 and Osborn’s model with a likely uncertainty of a factor of 4. L03 scaling can be used with a factor of proportionality five times that reported for the Baltic proper. Richardson number dependencies of the PP81 type can be employed if the background levels of eddy viscosity and diffusivity are increased to 1.3×10^{-3} and $1.3 \times 10^{-4} \text{ m}^2 \text{ s}^{-1}$, respectively. It should be emphasized that this is a local result, applicable to this environment. Thorpe scale-based estimates for dissipation can be made using Dillon’s constant of proportionality between Thorpe and Ozmidov scales (lies within 95% confidence intervals of our observations).

Examination of possible internal wave generation at the sill, its effects on mixing and overflow dynamics deserve further studies. A more thorough sampling of fine structure, LADCP in particular, as well as temporal coverage over several tidal cycles of both microstructure and fine structure is merited to attain more reliable conclusions and parameterizations.

Acknowledgments

This is publication number A101 of the Bjerknes Centre for Climate Research. Insightful and encouraging comments of three anonymous reviewers are greatly appreciated. IF is supported by the “Polar Ocean Climate Processes” (ProClim) project funded by the Norwegian Research Council, Grant 155923/700. Efforts of Pierre Jaccard, Steinar Myking and Tor Villy Kangas on operating MSS are appreciated. Yoshie Kasajima provided a preliminary version of LADCP data.

References

- Baker, M.A., Gibson, C.H., 1987. Sampling turbulence in the stratified ocean: statistical consequences of strong intermittency. *Journal of Physical Oceanography* 17, 1817–1836.
- Cairns, J.L., Williams, G.O., 1976. Internal wave observations from a midwater float, 2. *Journal of Geophysical Research* 81, 1943–1950.
- D’Asaro, E.A., Lien, R.-C., 2000. The wave-turbulence transition for stratified flows. *Journal of Physical Oceanography* 30, 1669–1678.
- Dillon, T.M., 1982. Vertical overturns: a comparison of Thorpe and Ozmidov length scales. *Journal of Geophysical Research* 87, 9601–9613.
- Fer, I., Skogseth, R., Haugan, P.M., Jaccard, P., 2003. Observations of the Storfjorden overflow. *Deep-Sea Research I* 50, 1283–1303.
- Fer, I., Skogseth, R., Haugan, P.M., 2004. Mixing of the Storfjorden overflow (Svalbard Archipelago) inferred from density overturns. *Journal Geophysical Research* 109, C01005.
- Galbraith, P.S., Kelley, D.E., 1996. Identifying overturns in CTD profiles. *Journal of Atmospheric and Oceanic Technology* 13, 688–702.
- Gargett, A.E., 1984. Vertical eddy diffusivity in the ocean interior. *Journal of Marine Research* 42, 359–393.
- Gargett, A.E., Holloway, G., 1984. Dissipation and diffusion by internal wave breaking. *Journal of Marine Research* 42, 15–27.
- Gargett, A.E., Hendricks, P.J., Sanford, T.B., Osborn, T.R., Williams, A.J., 1981. A composite spectrum of vertical shear in the upper ocean. *Journal of Physical Oceanography* 11, 1258–1271.
- Garrett, C.J., Munk, W.H., 1972. Space-time scales of internal waves. *Geophysical Fluid Dynamics* 2, 225–264.
- Garrett, C.J., Munk, W.H., 1975. Space-time scales of internal waves: a progress report. *Journal Geophysical Research* 80, 291–297.
- Gregg, M.C., 1977. Variations in the intensity of small-scale mixing in the main thermocline. *Journal of Physical Oceanography* 7, 436–454.
- Gregg, M.C., 1989. Scaling turbulent dissipation in the thermocline. *Journal of Geophysical Research* 94, 9686–9698.
- Gregg, M.C., Kunze, E., 1991. Shear and strain in Santa Monica Basin. *Journal Geophysical Research* 96, 16,709–16,719.
- Gregg, M.C., Sanford, T.B., Winkel, D.P., 2003. Reduced mixing from the breaking of internal waves in equatorial waters. *Nature* 422, 512–515.
- Henye, F.S., Wright, J., Flatté, S.M., 1986. Energy and action flow through an internal wave field: an eikonal approach. *Journal of Geophysical Research* 91, 8487–8495.
- Jungclaus, J.H., Backhaus, J.O., Fohrmann, H., 1995. Outflow of dense water from the Storfjord in Svalbard: a numerical model study. *Journal of Geophysical Research* 100, 24719–24728.
- Kozubskaya, G.I., Konyaev, G.V., Pludeman, A., Sabinin, K.D., 1999. Internal waves at the slope of Bear Island from the data of the Barents Sea Polar Front Experiment (BSPF-92). *Oceanology* 39, 147–154.
- Kunze, E., 1985. Near-inertial wave propagation in geostrophic shear. *Journal of Physical Oceanography* 15, 544–565.

- Kunze, E., Rosenfeld, L.K., Carter, G.S., Gregg, M.C., 2002. Internal waves in Monterey submarine canyon. *Journal of Physical Oceanography* 32, 1890–1913.
- Lass, H.U., Prandke, H., Liljebldh, B., 2003. Dissipation in the Baltic proper during winter stratification. *Journal Geophysical Research* 108, 3187.
- Leaman, K.D., Sanford, T.B., 1975. Vertical energy propagation of inertial waves: a vector spectral analysis of velocity profiles. *Journal of Geophysical Research* 80, 1975–1978.
- Levine, M.D., 2002. A modification of the Garrett–Munk internal wave spectrum. *Journal of Physical Oceanography* 32, 3166–3181.
- McComas, C.H., Müller, P., 1981. The dynamic balance of internal waves. *Journal of Physical Oceanography* 11, 970–986.
- Moum, J.N., 1996. Efficiency of mixing in the main thermocline. *Journal of Geophysical Research* 101, 12,057–12,069.
- Munk, W.H., 1966. Abyssal recipes. *Deep-Sea Research* 13, 707–730.
- Moum, J.N., Lueck, R.G., 1985. Causes and implications of noise in oceanic dissipation measurements. *Deep-Sea Research* 32, 379–390.
- Moum, J.N., Gregg, M.C., Lien, R.C., Carr, M.E., 1995. Comparison of turbulent kinetic energy dissipation rate estimates from two ocean microstructure profilers. *Journal of Atmospheric Oceanic Technology* 12, 346–366.
- Munk, W.H., 1981. Internal waves and small-scale processes. In: Warren, B.A., Wunsch, C. (Eds.), *Evolution of Physical Oceanography*. The MIT Press, Cambridge, pp. 264–290.
- Naveira Garabato, A.C., Oliver, K.I.C., Watson, A.J., Messias, M.-J., 2004a. Turbulent diapycnal mixing in the Nordic Seas. *Journal of Geophysical Research* 109, C12010.
- Naveira Garabato, A.C., Polzin, K.L., King, B.A., Heywood, K.J., Visbeck, M., 2004b. Widespread intense turbulent mixing in the Southern Ocean. *Science* 303, 210–213.
- Oakey, N.S., 1982. Determination of the rate of dissipation of turbulent energy from simultaneous temperature and velocity shear microstructure measurements. *Journal of Physical Oceanography* 12, 256–271.
- Oakey, N.S., Greenan, B.J.W., 2004. Mixing in a coastal environment: 2. A view from microstructure measurements. *Journal of Geophysical Research* 109, C10014.
- Osborn, T.R., 1980. Estimates of the local rate of vertical diffusion from dissipation measurements. *Journal of Physical Oceanography* 10, 83–89.
- Osborn, T.R., Cox, C.S., 1972. Oceanic fine structure. *Geophysics and Fluid Dynamics* 3, 321–345.
- Pacanowski, R.C., Philander, S.G.H., 1981. Parameterization of vertical mixing in numerical models of tropical oceans. *Journal of Physical Oceanography* 11, 1443–1451.
- Polzin, K.L., 2004. A heuristic description of internal wave dynamics. *Journal of Physical Oceanography* 34, 214–230.
- Polzin, K.L., Toole, J.M., Schmitt, R.W., 1995. Finescale parameterizations of turbulent dissipation. *Journal of Physical Oceanography* 25, 306–328.
- Polzin, K.L., Oakey, N.S., Toole, J.M., Schmitt, R.W., 1996. Fine structure and microstructure characteristics across the northwest Atlantic Subtropical Front. *Journal of Geophysical Research* 101, 14,111–14,121.
- Polzin, K.L., Kunze, E., Hummon, J., Firing, E., 2002. The finescale response of lowered ADCP velocity profiles. *Journal of Atmospheric and Oceanic Technology* 19, 205–224.
- Prandke, H., Stips, A., 1998. Test measurements with an operational microstructure turbulence profiler: detection limit of dissipation rates. *Aquatic Science* 60, 191–209.
- Quadfasel, D., Rudels, B., Kurz, K., 1988. Outflow of dense water from a Svalbard fjord into the Fram Strait. *Deep-Sea Research* 35, 1143–1150.
- Skogseth, R., Haugan, P.M., Haarpaintner, J., 2004. Ice and brine production in Storfjorden from four winters of satellite and in situ observations and modelling. *Journal of Geophysical Research* 109, C10008.
- Skogseth, R., Fer, I., Haugan, P.M., 2005a. Dense-water production and overflow from an Arctic coastal polynya in Storfjorden. In: Furevik, T., Drange, H., Dokken, T.M., Gerges, R., Berger, W. (Eds.), *The Nordic Seas: An Integrated Perspective*. AGU Geophysical Monograph Series 158, pp. 73–88.
- Skogseth, R., Haugan, P.M., Jakobsson, M., 2005b. Watermass transformations in Storfjorden. *Continental Shelf Research* 25, 667–695.
- Sternberg, R.W., Aagaard, K., Cacchione, D., Wheatcroft, R.A., Beach, R.A., Roach, A.T., Marsden, M.A.H., 2001. Long-term near-bed observations of velocity and hydrographic properties in the northeast Barents Sea with implications for sediment transport. *Continental Shelf Research* 21, 509–529.
- Stigebrandt, A., 1987. A model for the vertical circulation of the Baltic deep water. *Journal of Physical Oceanography* 17, 1772–1785.
- Stillinger, D.C., Helland, K.N., Van Atta, C.W., 1983. Experiments on the transition of homogeneous turbulence to internal waves in a stratified fluid. *Journal of Fluid Mechanics* 131, 91–122.
- Sun, H., Kunze, E., 1999. Internal wave-wave interactions: Part II. Spectral energy transfer and turbulence production rates. *Journal of Physical Oceanography* 29, 2905–2919.
- Thorpe, S.A., 1977. Turbulence and mixing in a Scottish loch. *Philosophical Transactions of the Royal Society of London A* 286, 125–181.
- Visbeck, M., 2002. Deep velocity profiling using lowered acoustic Doppler current profilers: bottom track and inverse solutions. *Journal of Atmospheric and Oceanic Technology* 19, 794–807.
- Vlasenko, V., Stashchuk, N., Hutter, K., Sabinin, K.D., 2003. Nonlinear internal waves forced by tides near the critical latitude. *Deep-Sea Research I* 50, 317–338.
- Wijesekera, H., Padman, L., Dillon, T., Levine, M., Paulson, C., 1993. The application of internal-wave dissipation models to a region of strong mixing. *Journal of Physical Oceanography* 23, 269–286.
- Yamazaki, H., Osborn, T., 1990. Dissipation estimates for stratified turbulence. *Journal of Geophysical Research* 95, 9739–9744.